






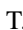



Single-particle and collective excitations in ^{66}Zn

A. D. Ayangeakaa ^{1,2,*} N. Sensharma ^{1,2,†} M. Fulghieri,^{1,2} R. V. F. Janssens ^{1,2} Q. B. Chen ³ S. Zhu,^{4,‡}
M. Alcorta,⁵ M. P. Carpenter ⁶ P. Chowdhury,⁷ A. Gade ^{8,9} C. R. Hoffman,⁶ F. G. Kondev ⁶
T. Lauritsen ⁶ E. A. McCutchan,⁴ A. M. Rogers ⁷ and D. Seweryniak⁶

¹*Department of Physics and Astronomy, University of North Carolina Chapel Hill, North Carolina 27599, USA*

²*Triangle Universities Nuclear Laboratory, Duke University, Durham, North Carolina 27708, USA*

³*Department of Physics, East China Normal University, Shanghai 200241, China*

⁴*National Nuclear Data Center, Brookhaven National Laboratory, Upton, New York 11973, USA*

⁵*TRIUMF, Vancouver, British Columbia, V6T 2A3, Canada*

⁶*Physics Division, Argonne National Laboratory, Argonne, Illinois 60439, USA*

⁷*Department of Physics, University of Massachusetts, Lowell, Massachusetts 01854, USA*

⁸*National Superconducting Cyclotron Laboratory, Michigan State University, East Lansing, Michigan 48824, USA*

⁹*Department of Physics and Astronomy, Michigan State University, East Lansing, Michigan 48824, USA*



(Received 14 April 2022; accepted 10 May 2022; published 23 May 2022)

Single-particle and collective excitations in ^{66}Zn have been investigated via the multinucleon transfer reaction, $^{26}\text{Mg}(^{48}\text{Ca}, \alpha 4n\gamma)$ using the Gammasphere multidetector array and the Fragment Mass Analyzer. In addition to confirming and complementing the previously known low-spin structure, a new quasirotational band comprising several stretched $E2$ transitions has been established to high spins. However, due to fragmentary nature of its decay, it was not possible to link this sequence to the low-lying states and, thus, determine the absolute excitation energies, spins, and parities unambiguously. Large-scale shell-model calculations employing the JUN45 and jj44b effective interactions are able to successfully describe the low-spin structure and herewith confirm that it is dominated by single-particle excitations. The newly established rotational cascade is compared with known superdeformed bands in the $A \approx 60\text{--}70$ mass region, and with results of calculations performed within the frameworks of the cranked shell model and the adiabatic and configuration-fixed constrained covariant density functional theory and the quantum particle-rotor model.

DOI: [10.1103/PhysRevC.105.054315](https://doi.org/10.1103/PhysRevC.105.054315)

I. INTRODUCTION

The underlying structure of nuclei in the $A \approx 60\text{--}70$ mass region provides opportunities to investigate the complex interplay between single-particle and collective degrees of freedom as a function of spin, N and Z . These nuclei are characterized by valence configurations in which the active orbitals correspond to the $\mathcal{N} = 3$ low- j pf , and the high- j $f_{7/2}$ subshells as well as the $\mathcal{N} = 4$ high- j , unique-parity $g_{9/2}$ orbital. The opposite deformation-driving effects of these orbitals play a major role in determining the structure and shape of these nuclei. On the one hand, the structure at low spin is dominated by single-particle and collective excitations generated primarily by valence nucleon excitations within the pf shell. On the other, collective excitations induced by multi-quasiparticle excitations across the $Z = 28$ shell gap into the $1g_{9/2}$ intruder orbital dominate at high angular momenta. These excitations have been linked, for example, to the appearance of highly deformed [1–8] and terminating bands

[9–12] as well as to the presence of strong magnetic dipole excitations [13,14] in the region. Indeed, due to the limited number of orbitals available near the Fermi level and the proximity to the $N = Z$ line, the observation of rotational bands with superdeformed characteristics in the $A \approx 60\text{--}70$ region remains of much interest for both experimental and theoretical studies.

In the present work, results of the investigation of the structure of ^{66}Zn , following a complex multinucleon transfer reaction $^{26}\text{Mg}(^{48}\text{Ca}, \alpha 4n\gamma)$, are presented. Previous spectroscopic studies of ^{66}Zn were undertaken in Refs. [15–19] and, very recently, by Bala *et al.* [20] and Rai *et al.* [21]. In the latter, a collective structure was observed up to termination accompanied by a crossing with the ground-state band around spin $6\hbar$. These observations have been confirmed and complemented with large-scale shell-model calculations carried out in the present work. In addition, by combining the experimental sensitivities of Gammasphere and the Fragment Mass Analyzer (FMA) with a novel experimental multinucleon transfer technique, a high-spin rotational cascade comprising of $\Delta I = 2$ transitions has been observed in coincidence with the low-spin structure. This sequence is observed to share characteristics similar to those of bands associated with superdeformation seen in neighboring nuclei of the

*ayangeak@unc.edu

†nsensharma@unc.edu

‡Deceased.

A ≈ 60 –70 region. Comparisons with calculations performed within the framework of the adiabatic and configuration-fixed constrained covariant density functional theory and the quantum particle rotor model suggest a configuration for the new band involving excitation of two protons from the $f_{7/2}$ into the $g_{9/2}$ subshells. Details of the present measurements and of the data analysis are given in Sec. II, while the discussion of the experimental results, and the description of theoretical calculations with shell-model and the combination of covariant density functional theory (CDFT) and particle-rotor model (PRM), are presented in Secs. III and IV, respectively.

II. EXPERIMENTAL DETAILS AND ANALYSIS

Medium and high-spin states in ^{66}Zn were populated via the $^{26}\text{Mg}(^{48}\text{Ca}, \alpha 4n\gamma)^{66}\text{Zn}$ multinucleon transfer reaction. A self-supporting 0.973-mg/cm^2 target of highly enriched ^{26}Mg was bombarded by ^{48}Ca ions at incident beam energies of 275, 290, and 320 MeV. These energies were provided by the ATLAS accelerator facility at the Argonne National Laboratory, and were chosen to be roughly 200% above the Coulomb barrier in order to favor multinucleon transfer and, in turn, enhance the population of high-spin yrast and near-yrast states. Gamma rays emitted in the de-excitation process were detected with Gammasphere [22,23], a 4π array of 101 Compton-suppressed high-purity germanium (HPGe) detectors. The reaction residues were transported to the focal plane of the FMA, where they were dispersed according to their mass-to-charge ratios, M/q . For this experiment, the FMA was tuned for the optimum transport of ions with an average charge state of 19^+ . The recoils were identified on an event-by-event basis from the position and time-of-flight measured in a microchannel plate detector (MCP) placed at the focal plane, and the energy loss measured with a three-fold segmented ionization chamber positioned behind the focal plane. The events were accumulated and recorded under the condition that recoil products be detected in kinematic coincidence with two or more γ rays within a 50-ns time window. More detailed information regarding the isotopic selection techniques, and the overall experimental procedure can be found in Ref. [24]. Gamma-ray events associated with ^{66}Zn recoils were sorted into fully symmetrized, two-dimensional (E_γ - E_γ) coincidence matrices while those arising from all Zn ions populated in the reaction were sorted into three-dimensional (E_γ - E_γ - E_γ) histograms. The latter were used mostly to confirm placements made using the former. The analysis was performed using the RADWARE suite of spectrum analyses packages [25].

Multipolarities for newly identified and previously known transitions were assigned on the basis of angular distribution measurements and, in the case of weak transitions, a two-point angular-correlation ratio, R_{ac} . The angular-distribution analysis was performed using coincidence matrices sorted such that energies of γ rays detected at specific Gammasphere angles (measured with respect to the beam direction) $E_\gamma(\theta)$, were incremented on one axis, while the energies of coincident γ rays detected at any angle, $E_\gamma(\text{any})$, were placed on the other. To improve statistics, adjacent rings of Gammasphere, and those corresponding to angles symmetric with respect to

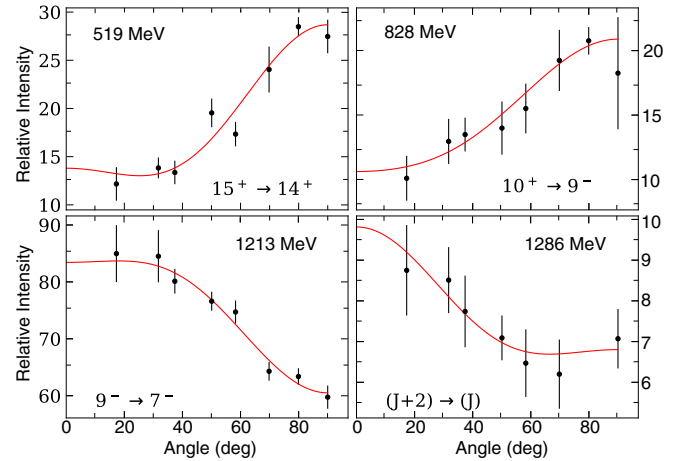


FIG. 1. Angular distributions for some of the γ transitions shown in the ^{66}Zn level scheme. Experimental data are shown as black circles while the angular distribution fit is given as a red curve.

90° in the forward and backward hemispheres, were combined. A total of seven matrices, with the angles 17.3° , 34.6° , 50.1° , 58.3° , 69.8° , 80.0° , and 90.0° [26] were created. By gating on the $E_\gamma(\text{any})$ axis and projecting on the $E_\gamma(\theta)$ axis, background-subtracted and efficiency-corrected spectra were generated. From these, the intensities of transitions of interest were extracted and fitted to the angular distribution function $W(\theta) = a_0[1 + a_2P_2(\cos\theta) + a_4P_4(\cos\theta)]$, where P_2 and P_4 are Legendre polynomials. The coefficients, a_2 and a_4 , containing information about the multipolarity of the transitions were extracted using an angular distribution code which uses the Markov chain Monte Carlo (MCMC) high-dimensional probability sampling technique [27]. Representative fits of angular distributions for some transitions of interest are displayed in Fig. 1.

Transitions for which an angular-distribution analysis was not possible, due mainly to limited statistics, a normalized ratio, R_{ac} , of γ -ray intensities observed in detectors in the forward (f)/backward (b) angles to the intensities in detectors centered around 90° was determined. For this purpose, two coincident matrices were incremented: In the first, $E_\gamma(f/b)$ vs $E_\gamma(\text{any})$, detectors in the forward and backward angles were combined and the matrix incremented such that γ rays detected at the 31.7° , 37.4° , 142.6° , 148.3° , and 162.7° angles were placed on one axis, with γ rays observed at any angle grouped along the other. The second matrix, $E_\gamma(\sim 90^\circ)$ vs $E_\gamma(\text{any})$, was incremented in a similar fashion, but with transitions observed in detectors at 79.2° , 80.7° , 90.0° , 99.3° , and 100.8° degrees placed on one axis. The two-dimensional angular correlation ratio, defined by $R_{ac} = I_\gamma(\theta_{f/b}, \text{any})/I_\gamma(\theta_{\sim 90^\circ}, \text{any})$, where $I_\gamma(\theta_x, \text{any})$ is the γ -ray intensity obtained by placing gates on the corresponding $E_\gamma(\text{any})$ axis. This ratio, which is independent of the multipolarity of the gating transition, was established to be greater than 1.0 for stretched-quadrupole transitions and less than 0.8 for stretched-dipole ones. Table I presents the energies, relative intensities, associated angular-distribution coefficients and R_{ac} ratios as well as the multipolarity assignments for the observed transitions.

TABLE I. Transition energies E_γ , relative intensities I_γ , angular distribution and correlation information for all transitions in ^{66}Zn . The intensities are corrected for detector efficiency and normalized to the 1038.5(4)-keV ground-state transition. R_{ac} is the normalized ratio of γ -ray intensities in the detectors at forward/backward angles to the intensities in the detectors at angles centered around 90° . The spin and excitation energy of Band 1 are based on $x \geq 10$ MeV and $J \geq 12$, as discussed in the text. All reported uncertainties are purely statistical in nature. Transitions marked with asterisk (*) are those for which the electric or magnetic character could not be confirmed in the present work. The assignments are taken from Refs. [20,21].

E_γ (keV)	I_γ	E_i (keV)	$I_i^\pi \rightarrow I_f^\pi$	a_2	a_4	R_{ac}	Mult.
175.9(3)	76.6(3)	4249.6(7)	$7^- \rightarrow 6^-$	-0.24(2)	-0.10(3)	0.84(1)	M1
312.0(1)	2.8(5)	3075.7(7)	$4^+ \rightarrow 4^+$	-	-	-	(M1/E2)
315.3(6)	3.4(9)	2763.8(6)	$4^+ \rightarrow 4^+$	-	-	-	(M1/E2)
327.7(1)	29.8(2)	4180.3(7)	$6^+ \rightarrow 6^+$	-	-	0.86(1)	M1
328.6(2)	83.2(4)	4073.5(6)	$6^- \rightarrow 5^-$	-0.22(1)	-0.06(2)	0.86(1)	M1
400.8(4)	2.4(6)	7915.7(1)	$12^+ \rightarrow 12^+$	-	-	0.9(1)	M1/E2
462.8(2)	4.2(9)	2773(2)	$(4^+) \rightarrow (3^+)$	-	-	0.8(5)	M1/E2
504.7(3)	88.4(3)	4249.6(7)	$7^- \rightarrow 5^-$	-	-	1.09(1)	E2
518.9(10)	24.1(1)	9820(2)	$15^+ \rightarrow 14^+$	-0.59(5)	0.26(8)	0.77(5)	M1/E2
577.0(4)	4.0(6)	2448.5(6)	$4^+ \rightarrow 2^+$	-	-	1.26(2)	E2
627.3(10)	24.1(2)	3075.7(7)	$4^+ \rightarrow 4^+$	-0.28(6)	-0.57(9)	1.11(4)	M1/E2
643.2(5)	3.1(6)	5204.9(7)	$8^+ \rightarrow 6^+$	0.54(14)	0.07(21)	1.54(4)	E2
644.3(5)	1.43(6)	7514.9(10)	$12^+ \rightarrow 11^-$	-	-	0.91(13)	E1*
669.3(8)	27.5(14)	3744.7(6)	$5^- \rightarrow 4^+$	-0.37(4)	-0.06(5)	0.85(4)	E1*
738.4(2)	10.3(10)	6076(2)	$9^- \rightarrow 8^-$	-	-	0.91(1)	M1/E2
755.8(3)	6.5(12)	3066(2)	$(5^+) \rightarrow (3^+)$	-	-	1.16(5)	E2
758.0(8)	0.16(10)	3521.8(1)	$\rightarrow 4^+$	-	-	-	-
828.1(1)	19(1)	6290.2(8)	$10^+ \rightarrow 9^-$	-0.45(7)	0.09(11)	0.89(6)	E1*
830.7(8)	7(1)	2702.3(1)	$3^+ \rightarrow 2^+$	-	-	0.78(5)	M1/E2
833.2(4)	23.2(4)	1871.6(6)	$2^+ \rightarrow 2^+$	-	-	0.79(5)	M1
855.5(10)	3.1(9)	7145.7(1)	$12^+ \rightarrow 10^+$	-	-	1.46(34)	E2
860.8(8)	2.4(10)	5109.6(7)	$8^- \rightarrow 7^-$	-	-	0.86(14)	M1/E2
863.2(3)	4.7(8)	3929(2)	$(7^+) \rightarrow (5^+)$	-	-	1.21(4)	E2
892.3(3)	11(1)	2763.8(6)	$4^+ \rightarrow 2^+$	-	-	1.35(18)	E2
919.9(3)	6.6(8)	3744.7(6)	$5^- \rightarrow 3^-$	-	-	1.17(14)	E2
943.8(4)	1(1)	3707.6(1)	$\rightarrow 4^+$	-	-	-	-
953.7(1)	1.2(9)	2824.7(6)	$3^- \rightarrow 2^+$	-	-	-	(E1*)
954.2(5)	45.9(2)	5204.9(7)	$8^+ \rightarrow 7^-$	-0.38(2)	-0.04(3)	0.80(2)	E1*
981.3(2)	7.8(8)	3744.7(6)	$5^- \rightarrow 4^+$	-	-	0.76(11)	E1*
1025.8(5)	30.2(3)	5204.9(7)	$8^+ \rightarrow 6^+$	-	-	1.16(3)	E2
1036.0(3)	56.4(3)	5109.6(7)	$8^- \rightarrow 6^-$	-	-	1.21(5)	E2
1038.5(4)	207.4(9)	1038.5(4)	$2^+ \rightarrow 0^+$	0.10(2)	-0.08(2)	1.07(1)	E2
1085.3(4)	66.0(3)	6290.2(8)	$10^+ \rightarrow 8^+$	-	-	1.22(2)	E2
1087.8(5)	3.1(9)	5337.3(10)	$8^- \rightarrow 7^-$	-	-	-	(M1/E2)
1089.3(10)	1.7(1)	12276(2)	$17^+ \rightarrow 16^+$	-	-	0.70(19)	M1/E2
1204.2(5)	8.9(10)	3075.7(7)	$4^+ \rightarrow 2^+$	-	-	1.09(7)	E2
1212.5(4)	57.8(3)	5462.1(8)	$9^- \rightarrow 7^-$	0.25(3)	-0.09(4)	1.20(1)	E2
1224.7(7)	48.3(2)	7514.9(10)	$12^+ \rightarrow 10^+$	0.15(3)	-0.13(4)	1.13(3)	E2
1263.9(3)	5.1(1)	5337.3(10)	$8^- \rightarrow 6^-$	0.16(9)	-0.13(12)	1.35(12)	E2
1271.0(10)	7.9(5)	9820(2)	$15^+ \rightarrow (14^+)$	-	-	-	-
1271.9(2)	3.5(3)	2310.4(1)	$(3^+) \rightarrow 2^+$	-	-	-	-
1284.8(3)	6.9(9)	4058.0(1.9)	$(6^+) \rightarrow (4^+)$	-	-	1.24(10)	E2
1286.0(5)	5.3(3)	$x + 1286.0$	$J+2 \rightarrow J$	0.22(10)	0.14(12)	1.27(1)	E2
1295.6(4)	90.9(4)	3744.7(6)	$5^- \rightarrow 4^+$	-0.32(2)	-0.05(2)	0.75(2)	E1*
1307.1(7)	9.5(4)	6416.7(1)	$\rightarrow 8^-$	-	-	-	-
1366.6(2)	6.3(8)	11186.5(2)	$16^+ \rightarrow 15^+$	-	-	0.77(17)	M1/E2
1385.3(5)	2.6(5)	9301.0(1)	$14^+ \rightarrow 12^+$	-	-	1.21(22)	E2
1399.4(3)	5.7(7)	12275.8(2)	$17^+ \rightarrow 16^+$	-	-	-	(M1/E2)
1404.2(1)	22.6(3)	3852.6(1)	$6^+ \rightarrow 4^+$	-	-	1.21(54)	E2
1408.5(2)	30.2(2)	6870.6(1)	$11^- \rightarrow 9^-$	-	-	1.14(4)	E2
1410.3(8)	132.0(8)	2448.5(6)	$4^+ \rightarrow 2^+$	0.22(4)	0.01(6)	1.14(1)	E2
1432.4(4)	4.2(2)	$x + 2718.4$	$J+4 \rightarrow J+2$	-	-	1.17(12)	E2

TABLE I. (*Continued.*)

E_γ (keV)	I_γ	E_i (keV)	$I_i^\pi \rightarrow I_f^\pi$	a_2	a_4	R_{ac}	Mult.
1457.6(5)	2.2(6)	5515.6(2)	$(8^+) \rightarrow (6^+)$	–	–	1.33(11)	$E2$
1484.2(2)	0.5(4)	12670.8(2)	$17^+ \rightarrow 16^+$	–	–	0.78(14)	$M1/E2$
1486.2(5)	2.9(12)	4561.8(1)	$6^+ \rightarrow 4^+$	–	–	1.29(15)	$E2$
1508.0(8)	2(1)	9022.9(2)	$14^+ \rightarrow 12^+$	–	–	1.22(43)	$E2$
1537.0(6)	2.2(6)	7612.7(2)	$11^- \rightarrow 9^-$	–	–	1.17(41)	$E2$
1575.5(2)	6.7(9)	10876.4(2)	$16^+ \rightarrow 14^+$	0.19(14)	0.02(18)	1.20(11)	$E2$
1625.2(2)	11.2(11)	7915.7(1)	$12^+ \rightarrow 10^+$	0.21(10)	–0.10(15)	1.16(9)	$E2$
1628.7(5)	3.9(1)	$x + 4347.1$	$J+6 \rightarrow J+4$	–	–	1.27(15)	$E2$
1656.1(2)	0.7(5)	9268.8(2)	$13^- \rightarrow 11^-$	–	–	1.28(20)	$E2$
1725.4(4)	25.8(3)	2763.8(6)	$4^+ \rightarrow 2^+$	–	–	1.26(4)	$E2$
1732.9(5)	34.3(2)	4180.3(7)	$6^+ \rightarrow 4^+$	–	–	1.25(4)	$E2$
1785.3(7)	10.6(4)	2824.7(6)	$3^- \rightarrow 2^+$	–	–	–	$(E1^*)$
1786.1(2)	19.4(2)	9301.0(1)	$14^+ \rightarrow 12^+$	–	–	1.23(8)	$E2$
1801.0(5)	4.1(8)	8671.6(2)	$13^- \rightarrow 11^-$	–	–	1.20(31)	$E2$
1832.1(4)	4.4(9)	$x + 6179.2$	$J+8 \rightarrow J+6$	–	–	1.30(16)	$E2$
1925.5(1)	1(1)	11226.5(2)	$(16^+) \rightarrow 14^+$	–	–	–	$(E2)$
2040.3(7)	2.1(7)	$x + 8219.5$	$J + 10 \rightarrow J + 8$	–	–	1.23(19)	$E2$
2215.3(4)	0.7(4)	$x + 10434.8$	$J + 12 \rightarrow J + 10$	–	–	–	$E2$
2423.4(7)	1.0(4)	$x + 12858.2$	$J + 14 \rightarrow J + 12$	–	–	–	$E2$
2679.4(4)	0.19(3)	$x + 15537.6$	$J + 16 \rightarrow J + 14$	–	–	–	$E2$
2933.1(4)	0.1(9)	$x + 18470.7$	$(J + 18) \rightarrow J + 16$	–	–	–	–

III. RESULTS

The level scheme resulting from the coincidence analysis of γ rays associated with ^{66}Zn recoils is displayed in Fig. 2. It was constructed primarily based on coincidence relationships and relative intensity balances using the γ - γ matrix gated on ^{66}Zn recoils and crosschecked, for intense transitions, using a γ - γ - γ cube constructed from all Zn events produced in the reaction. The level scheme features two primary structures; a low-to-medium spin one (shown on the right) and a newly established high-spin rotational sequence composed of stretched- $E2$ transitions, displayed on the left. As noted above, the low-to-medium spin structure, up to the 12_1^+ level at 7514.9(10) keV, was previously established in Refs. [15–19]. The observations are confirmed here. While the present work was in preparation, Rai *et al.* [21] and Bala *et al.* [20] independently reported the observation of additional new excited states in ^{66}Zn . Using a heavy-ion induced reaction, Rai *et al.* [21] added positive-parity levels connected by the 519-, 1089-, 1367-, 1399-, 1576-, and 1786-keV transitions above the 12_1^+ state, and two new transitions (1408 and 1801 keV) in the negative-parity part, as well as the 644- and 828-keV transitions linking the two sequences. This established the structure up to an excitation energy of ≈ 12.3 MeV and a spin of $\approx 17\hbar$. These transitions, some of which are highlighted with red squares in the total projection spectrum displayed in Fig. 3, and their placements are also confirmed in the present work. Indeed, this work validates almost all placements within this structure and agrees with the multipolarity assignments for the newly identified transitions associated with the positive-parity levels reported by Rai *et al.* [21]. It, however, differs somewhat in the placement and multipolarity assignments for the 738-, 1264-, and 1537-keV transitions linking the negative-parity states. For example, the 738-keV transition, of dipole

character, is placed in Ref. [21] as feeding directly the 6_1^- level at 4074 keV, bypassing the 4250-keV 7_1^- state and thus, in anticoincidence with the 176-keV γ ray. In the present work, the 738-keV transition is found to directly populate the 8^- level at 5338 keV, which is in turn depopulated by two transitions; a 1264-keV quadrupole one (reported as dipole in Ref. [21]) to the 4074-keV 6_1^- level, and a 1088-keV one (not seen in Ref. [21]) to the 7_1^- state at 4250 keV. A γ - γ coincidence spectrum, obtained by gating on the 738-keV γ ray (see Fig. 4) exhibits a coincidence relationship between the 738- and 176-keV transitions. This, along with the presence of a 1088-keV γ ray in the 176-keV gate, and the absence of coincidence relationships between the 1264- and 176-keV lines, supports the assignment of the 738-keV γ ray as the link between the 6076(2) 9^- and 5337.3(10)-keV 8^- states. As depicted in Fig. 2, energy sums and intensity balances suggest the population and depopulation of the 8^- , 5337.3(10)-keV level by the 738- and 1264-keV γ rays, respectively, in contrast with the reverse order suggested in Ref. [21]. It should be noted that none of the new transitions reported in Ref. [20] following the $^{56}\text{Fe}(^{12}\text{C}, 2p\gamma)$ fusion-evaporation reaction is observed in the present work.

The rotational sequence identified as Band 1 in Fig. 2 is newly established. It consists of nine transitions; i.e., the 1286-, 1432-, 1629-, 1832-, 2040-, 2215-, 2423-, 2679-, and (2933-) keV γ rays. A summed coincidence spectrum obtained by individually gating on all the in-band transitions is presented in Fig. 5. This spectrum highlights an almost constant energy spacing, ΔE_γ , between these γ rays, which suggests the onset of collectivity. While it was not possible to connect it directly to the low-to-medium spin structure of Fig. 2, presumably because of the low intensities and possible fragmented decay paths, Band 1 is assigned to ^{66}Zn based on

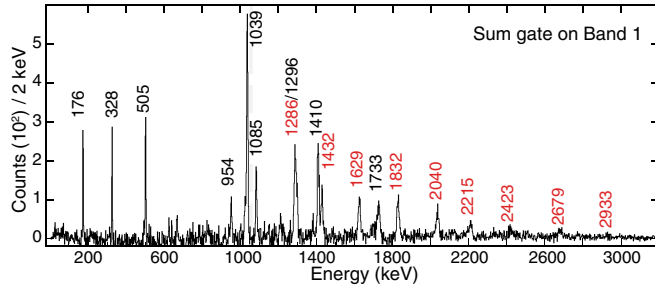


FIG. 5. Sum of single coincidence gates placed on γ -ray transitions in band 1. Pertinent γ rays are highlighted in red.

structure and equilibrium shape of the nucleus. In neutron-rich Zn isotopes, the rotational alignment of $\pi g_{9/2}$ and/or $\nu g_{9/2}$ intruder orbitals, which come progressively closer to the Fermi level with increasing neutron excess, give rise to a significant increase in aligned angular momentum, resulting in the appearance of a large variety of deformed, collective excitations as observed in several nuclei of the $A \approx 60$ –70 mass region [3–6,8,10]. At low spins, however, the structure is dominated by single-particle type excitations involving a few nucleons as a result of their proximity to the $Z = 28$ shell closure. In this section, the low-spin structure of ^{66}Zn nucleus, with two protons and eight neutrons outside the doubly magic core, ^{56}Ni , is investigated by comparing the data with results of large-scale shell-model calculations. The rotational characteristics of the high-spin structure, on the other hand, are compared with similar bands observed in the region and discussed within the framework of the combination of constrained covariant density functional theory (CDFT) and particle-rotor model (PRM) as well as the cranked shell model (CSM).

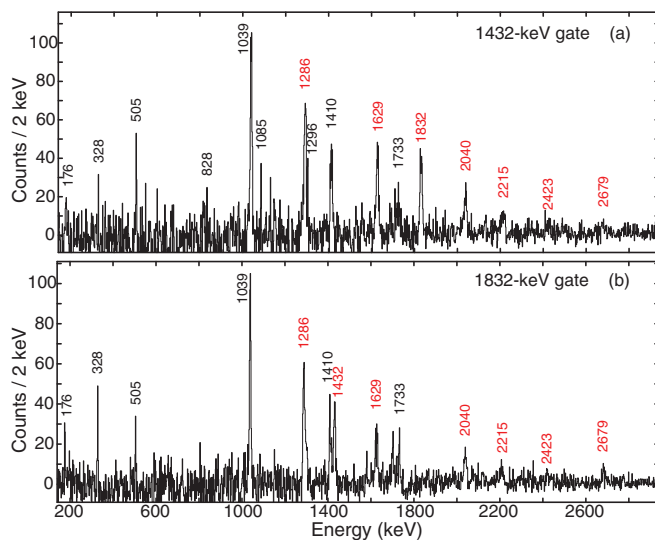


FIG. 6. Coincidence spectra obtained by single gating on transitions at (a) 1432 keV and (b) 1832 keV. Members of the rotational band are marked in red.

A. Low-spin excitations

Several theoretical approaches, such as the shell model [28,29] and its deformed configuration mixing variant [30], the cluster vibration model [31,32], and a microscopic description within the framework of the Hartree-Fock-Bogoliubov approximation [33] have been previously employed to investigate the structure of low-lying states in ^{66}Zn . In Ref. [30], the yrast structure is calculated to be composed of two parts; the ground-state sequence with $J^\pi = 0^+$, 2^+ , 4^+ , 6^+ described as resulting predominantly from the $\pi \nu(p_{3/2}, f_{5/2}, p_{1/2})^{10}$ configuration, and a series of excited states with $J^\pi = 8^+$, 10^+ , 12^+ , 14^+ , belonging mainly to the $2p$ - $2h$ $\pi(p_{3/2}, f_{5/2}, p_{1/2})^8 \otimes \nu(g_{9/2})^2$ configuration, which is associated with a small deformation. These two modes of excitation are found to cross (see Fig. 8) as a result of the two particle-hole excitation involving the neutron $1g_{9/2}$ orbital. Thus, in the total Routhian surface (TRS) calculations of Ref. [21], the crossing is attributed to the alignment of a pair of neutrons which drives the ^{66}Zn nucleus from an oblate shape in the ground state via the triaxial shape at the intermediate spin to a collective prolate shape at high spin.

In the present study, the nature of the ^{66}Zn low-lying states has been investigated by means of a configuration interaction calculations in the $jj44$ model space which comprises the $0f_{7/2}$, $1p_{3/2}$, $1p_{1/2}$, and $0g_{9/2}$ orbitals for both protons and neutrons and assumes a ^{56}Ni inert core. The calculations were performed using the shell-model code NUSHELLX [34] with an isoscalar effective charge of $e_\pi + e_\nu = 2.6$ and two effective interactions tuned for the $f_{5/2}pg_{9/2}$ model space—the $jj44b$ and JUN45 Hamiltonians. These interactions have been extensively used to study low-lying structures in nuclei of the $A \approx 60$ –70 region, and were able to reproduce the general features exhibited by the data quite well.

The results of shell-model calculations using both sets of interactions are compared with the ^{66}Zn experimental excitation energies for the yrast and near-yrast states in Fig. 7. For clarity, the positive- and negative-parity states have been separated into two groups and, in the calculated spectra, only the lowest-energy levels for each spin with corresponding experimental states are presented. The yrast levels are indicated by red lines. As can be seen, the yrast structure is reproduced well by both interactions for excitation energies below ~ 6 MeV, thus indicating a predominately spherical or nearly spherical character at low spin. The limited number of valence particles available outside the spherical ^{56}Ni core implies that the low-lying structure will be dominated by spherical shell-model states. This is particularly evident in the calculations, as the 2_1^+ level energy is predicted to within 13 and 20 keV of the experimental value of 1039 keV by the $jj44b$ and JUN45 interactions, respectively. Likewise, the experimental 4_1^+ state at 2449 keV is reproduced by the calculations, with the JUN45 interaction performing slightly better (2451 keV) than the $jj44b$ (2272 keV) one. Overall, the yrast sequence of states comprising the 2_1^+ , 4_1^+ , 6_1^+ , 8_1^+ , and 10_1^+ at 1039, 2449, 4180, 5205, and 6290 keV is reproduced better by the JUN45 interaction as illustrated in Fig. 8, although the $jj44b$ predictions remain within 200 keV of the experimental values. This is not surprising since ^{66}Zn is one of the nuclei to which the

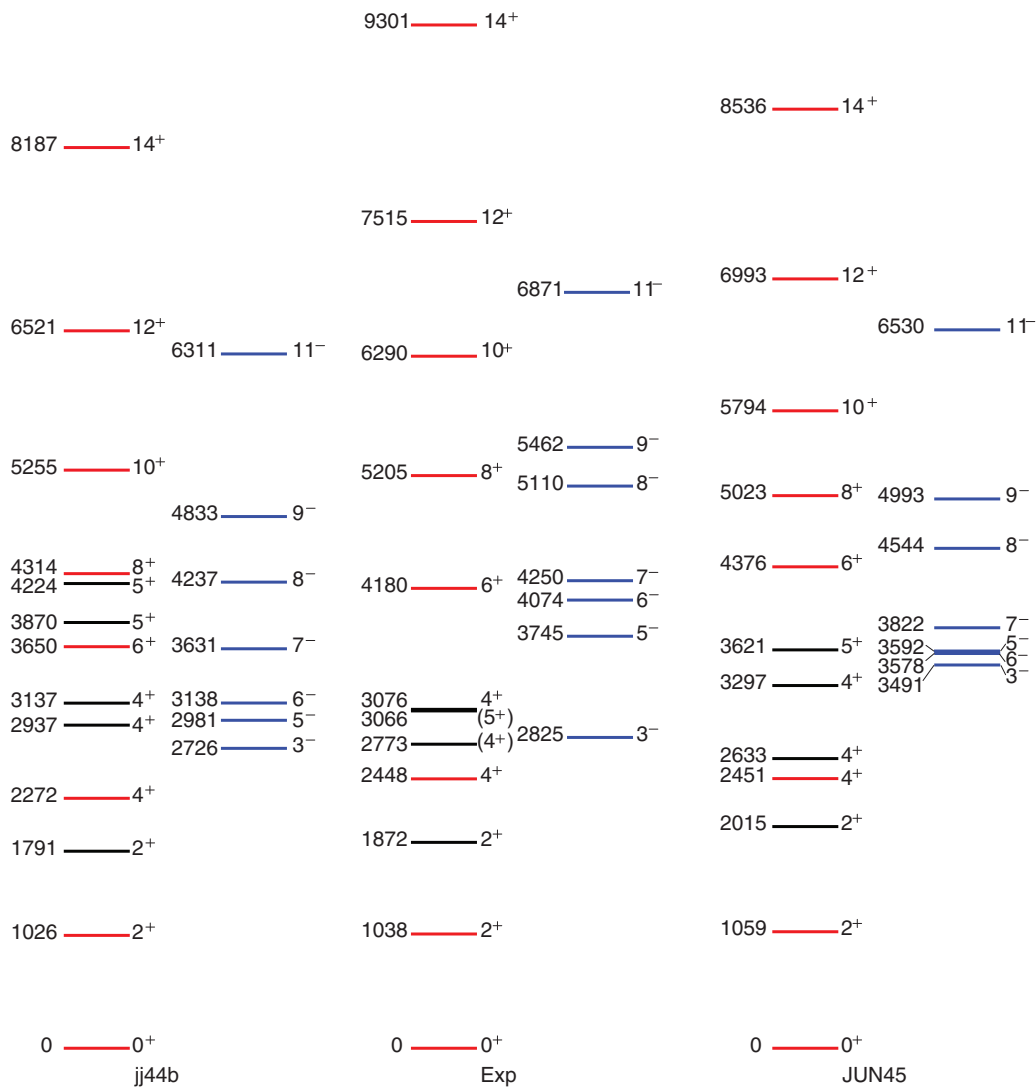


FIG. 7. Experimental level energies in ^{66}Zn compared with spherical shell-model calculations using the jj44b and JUN45 effective interactions. The yrast levels are indicated by the red lines while the negative structure is colored dark blue.

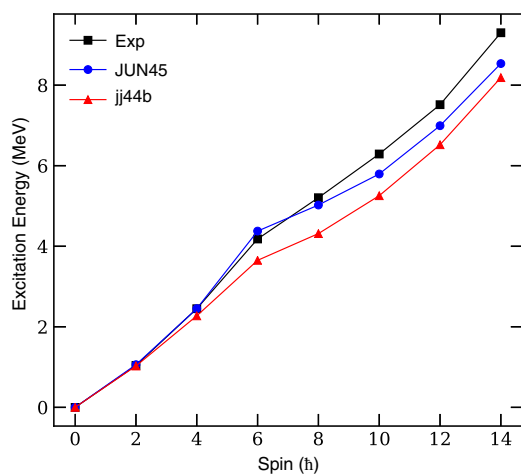


FIG. 8. Comparison of the yrast level energies in ^{66}Zn with spherical shell-model states calculated using the jj44b and JUN45 effective interactions (see text for details).

effective single-particle energies (ESPE) and two-body matrix elements (TBME) for both the JUN45 and jj44b Hamiltonians were empirically adjusted in order to fit the experimental binding and excitation energies. For the yrast and near-yrast states, the two interactions predict a predominantly mixed $\pi(f_{5/2})^2 \otimes \nu(p_{1/2}, f_{5/2}, p_{3/2})^8$ configuration with minimal contribution ($\sim 4\%$ probability) from the $\pi(f_{5/2}, p_{3/2})^2 \otimes \nu(p_{1/2}, f_{5/2}, p_{3/2}, g_{9/2})^8$ component. The contribution of the latter increases in amplitude towards higher spins. The average neutron occupation of the $\nu g_{9/2}$ orbital increases from 0.8 for the 0_1^+ state (in agreement with single-neutron pickup data indicating a particle occupation number in the ground state of at least 0.7 for this $g_{9/2}$ state [35,36]) to about 1.29 while that for the proton decreases from 0.10 (0_1^+ state) to 0.06 (10_1^+ level) in the JUN45 calculations. A similar trend is observed in the jj44b computations. Beyond the 10_1^+ state, the divergence between the calculated and experimental yrast states becomes significant, with both interactions systematically underpredicting the experimental observations (see

Fig. 8). As discussed below, this could be due to the increasing role of collective excitations at high angular momenta. Theoretical predictions for the nonyrast states, indicated by black lines in Fig. 7, follow a pattern similar to those for the yrast states; i.e., the calculations predict the energies of the low-lying states well, but underestimate (overestimate in the case of jj44b) the experimental energies at high spin. This is apparent in Fig. 7 as both interactions predict the excitation energy of the 2_2^+ and 4_2^+ states well, but fail at higher energies. For the 2_2^+ state, a predominantly $\pi(f_{5/2}, p_{3/2})^2 \otimes \nu(p_{1/2}, f_{5/2}, p_{3/2}, g_{9/2})^8$ configuration (46%) is predicted while the $\pi(f_{5/2}, p_{3/2})^2 \otimes \nu(p_{1/2}, f_{5/2}, p_{3/2}, g_{9/2})^8$ component is about 2%. The latter configuration is calculated to become the leading component with 18% probability in the 4_2^+ state. Similarly, the 2825-keV excitation energy of the $I^\pi = 3^-$ state is reproduced well by the jj44b interaction which is calculated to within ~ 100 keV of the experimental value. The overall good agreement between calculations and experimental levels demonstrates that the low-spin structure is predominantly of single-particle character and is, thus, consistent with the expectation that the limited number of valence particles outside of doubly magic ^{56}Ni allows for a low angular momentum structure dominated by spherical shell-model states.

B. High-spin structure

The results of the previous section indicate that, as is the case for most nuclei in the $A \approx 60\text{--}70$ mass region, the ^{66}Zn low-spin structure is determined primarily by excitations involving the $1f_{5/2}$, $2p_{3/2}$, and $2p_{1/2}$ single-particle levels with minimal contributions from the intruder $1g_{9/2}$ orbital. With increasing spin, contributions from both neutron and proton occupation of this shape-driving $1g_{9/2}$ intruder orbital become significant, thereby enhancing the possibility of observing deformed shapes as well as the onset of specific collective rotational behavior such as that manifested through rotational sequences such as smoothly terminating, highly deformed, and superdeformed (SD) bands. Microscopically, the emergence of SD bands in this mass region is understood as a result of multiple excitations of $\pi f_{7/2}$ and $\nu f_{7/2}$ particles/holes into the shape driving $\pi g_{9/2}$ and $\nu g_{9/2}$ intruder orbitals. In a manner consistent with theoretical predictions of SD shell gaps at particle numbers $N, Z = 30, 32$ [37], rotational bands associated with superdeformation have been reported in several isotopes of Zn and Ge, thus enabling a systematic study of highly deformed shapes in nuclei with $N \approx Z$. In the case of the Zn isotopes, bands with SD properties have been observed in $^{60\text{--}63, 65, 68}\text{Zn}$ [3–6], with the exception of $^{64, 66, 67}\text{Zn}$. Lifetime measurements in several of these nuclei support the interpretation that these bands are characterized by unusually large deformations. For instance, an average transition quadrupole moment, Q_t , of $3.0_{-0.4}^{+0.5}$ eb has been reported in ^{61}Zn [5]. This corresponds to a quadrupole deformation of $0.50_{-0.06}^{+0.07}$, when assuming an axially symmetric shape. Calculations within the Hartree-Fock formalism suggest that this band most likely has the $(\nu g_{9/2})^3(\pi g_{9/2})^2$ configuration. For the SD band in ^{62}Zn , a quadrupole moment of $2.7_{-0.5}^{+0.7}$ eb, corresponding to a deformation $\beta_2 = 0.45_{-0.07}^{+0.10}$ [8], has been

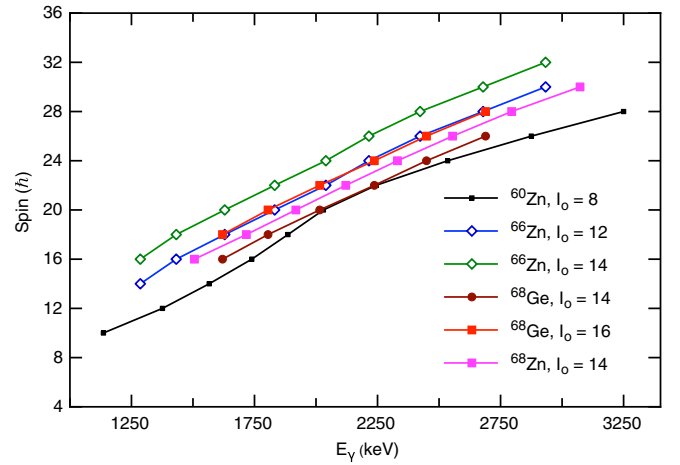


FIG. 9. Angular momentum as a function of transition energy for the superdeformed bands in ^{60}Zn , ^{68}Zn , and ^{68}Ge compared with the newly established band in ^{66}Zn . The data for ^{68}Ge and ^{66}Zn are plotted for band head spins of $I_0 = 14$ and $I_0 = 16$, and $I_0 = 12$ and $I_0 = 14$, respectively (see text for details).

measured. Similar deformation parameters have been found in $^{60, 68}\text{Zn}$ [3, 6]. While the SD bands observed in $^{60, 61}\text{Zn}$ have been linked to the states of lower spin, those reported in $^{63, 65, 68}\text{Zn}$ have not, potentially due to the fragmentation of strength associated with the decay out of the SD band.

It is within this context that a closer examination of the behavior of the rotational band observed in the present work becomes important. Figure 9 presents a plot of the angular momentum as a function of transition energy for the SD bands in $^{60, 68}\text{Zn}$ [3, 6] and ^{68}Ge [12], the $N = 36$ isotone of ^{66}Zn , compared with the band established in this work. Due to lack of knowledge of the absolute excitation energies and spins, the data for ^{68}Ge and ^{66}Zn are plotted for two band head spins, $I_0 = 14$ and $I_0 = 16$, and $I_0 = 12$ and $I_0 = 14$, respectively. Furthermore, following the approach of Ref. [12], the transition energies for the band in ^{60}Zn have been scaled by $(60/66)^{5/3}$ to account for the expected mass dependence of the moments of inertia. As can be seen from Fig. 9, the slope, which characterizes the moment of inertia, is similar for all the bands. In particular, the variation in the angular momentum as a function of γ -ray energy for band 1 (in ^{66}Zn) and the SD band in ^{68}Ge follow the same trend, especially if the band head spins are taken as $12\hbar$ and $16\hbar$, respectively. This likely suggests a similar intrinsic configuration. To highlight this similarity further, the SD band in ^{68}Ge is plotted alongside the ^{66}Zn rotational sequence in Fig. 10. Note that the striking similarities between the levels of ^{66}Zn and ^{68}Ge has been extensively discussed in Ref. [21], albeit for lower spin states. Theoretical calculations for all the cases presented in Fig. 9, as well as for the known SD bands in $^{63, 65}\text{Zn}$ [5], indicate that the band configurations involve at least two proton holes in the $f_{7/2}$ subshell and it is, thus, reasonable to expect that the band in ^{66}Zn is based on a similar configuration as well.

Since no direct linking to the low-energy levels is observed, only the dynamic moment of inertia $\mathcal{J}^{(2)}$, which is strongly influenced by the alignment of high- j configurations, can

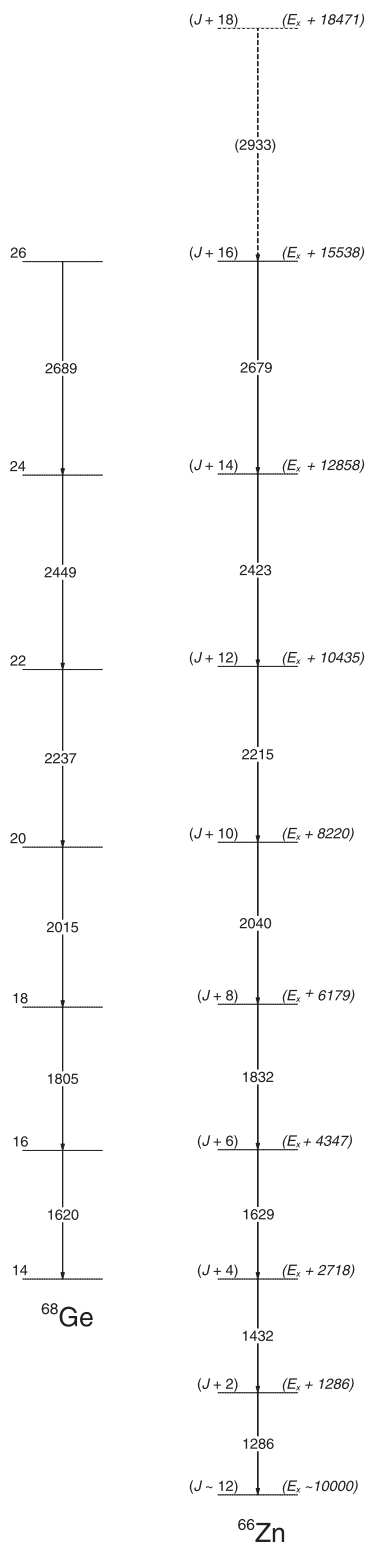


FIG. 10. Comparison of the rotational band in ^{66}Zn with the SD sequence in ^{68}Ge . The data for ^{68}Ge are taken from Ref. [12].

be extracted from the experimental data with certainty. This moment is plotted for the newly established band in ^{66}Zn as a function of the rotational frequency, $\hbar\omega$, alongside those of $^{60,68}\text{Zn}$ and ^{68}Ge in Fig. 11. In contrast to the SD band in ^{68}Zn ,

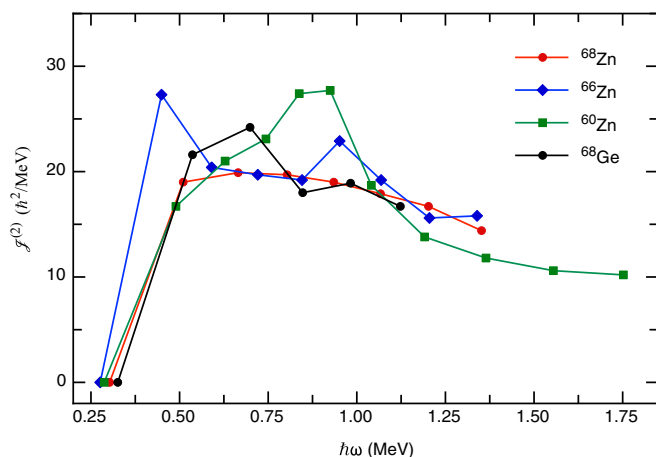


FIG. 11. Variation of the experimentally deduced dynamic moment of inertia as a function of the rotational frequency ($\hbar\omega$) for Band 1 in ^{66}Zn (present work), compared with known SD bands in the neighboring ^{68}Ge [12] and $^{60,68}\text{Zn}$ [3,6].

which displays a regular, smooth decrease with increasing rotational frequency, the $\mathcal{J}^{(2)}$ moments for $^{60,66}\text{Zn}$ and ^{68}Ge exhibit a more staggering behavior, with pronounced peaks at certain frequencies. For ^{60}Zn , the rise in the $\mathcal{J}^{(2)}$ moment of inertia at $\sim 0.9 \hbar\omega$ has been interpreted as the simultaneous alignment of the $g_{9/2}$ protons and neutrons [3], mediated by various components of the nucleon-nucleon interaction. A detailed systematic analysis of the $\mathcal{J}^{(2)}$ moments of inertia for bands in $^{60-65}\text{Zn}$ [5] indicates that the rise cannot only be attributed to changes in nn or pp pairing, but rather involves a significant np component as the main cause for the enhancement. These studies further suggest that the rise appears only when the occupation of the $g_{9/2}$ intruder states is identical for valence protons and neutrons. It is, thus, conceivable that the enhancements observed in ^{66}Zn and ^{68}Ge at about the same frequency ($\sim 0.9 \hbar\omega$), but reduced strength, can be attributed to similar configurations undergoing such interactions.

To understand these interactions, the alignment properties of the rotational sequence observed in ^{66}Zn were investigated within the framework of the cranked shell model (CSM). The calculations were performed for both quasiprotons and quasineutrons with the associated single-particle level energies determined using a deformed Woods-Saxon potential with universal parameters. For the present calculation, the deformation parameter set ($\beta_2 = 0.4$, $\beta_4 = 0.0$, and $\gamma = 23^\circ$) was chosen to correspond with those of the highly deformed bands in the region [12]. The pairing energies at zero frequency $\Delta_n(\omega = 0) = 1.4542 \text{ MeV}$ and $\Delta_p(\omega = 0) = 0.6473 \text{ MeV}$ were determined using the BCS formalism and kept constant as a function of frequency. The resulting quasiproton Routhian is presented in Fig. 12 with the relevant quasiparticle orbitals (i.e., those near the Fermi surface) labeled according to the convention of Ref. [38]. The calculation predicts an AB crossing, corresponding to the alignment of a pair of $g_{9/2}$ protons, at a frequency ($\sim 0.63 \text{ MeV}/\hbar$) lower than the point to which the available data for Band 1 extend and hence, is unlikely to be observed in the present measurement.

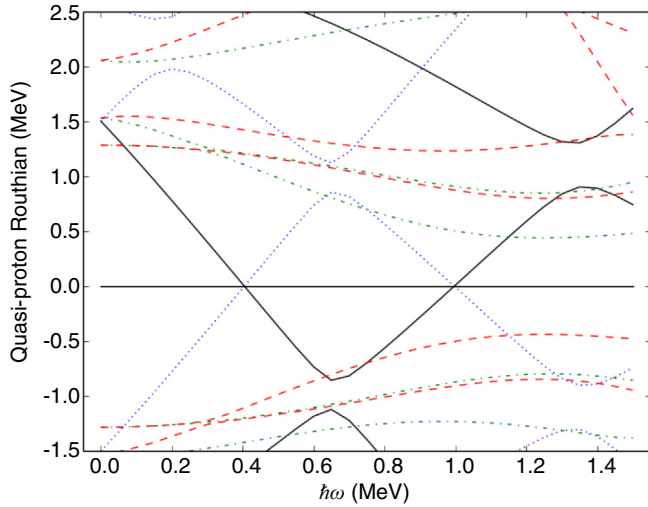


FIG. 12. The calculated quasiproton Routhian (e') as a function of rotational frequency ($\hbar\omega$). The following convention is adopted for the parity and signature (π, α) of the Routhians: (+, 0) solid lines, (+, 1) dotted lines, (-, 0) dash-dotted lines, and (-, 1) dashed lines.

To gain further insight, the rotational characteristics of Band 1 in ^{66}Zn was analyzed with the help of the adiabatic and configuration-fixed constrained covariant density functional theory (CDFT) [39–41] and the quantum particle rotor model (PRM) formalism [42–44]. First, the former approach was used to search for possible configurations and deformations associated with the band. In the calculations, the point-coupling effective interaction PC-PK1 [45], with a basis of ten major oscillator shells, was employed, while the pairing correlations were neglected for simplicity. It was found that the ground state of ^{66}Zn is triaxial with deformation parameters ($\beta = 0.19, \gamma = 29^\circ$). Based on this state and by always keeping two aligned neutrons or protons in the first and second states of the $g_{9/2}$ shell while the other nucleons fill the orbitals according to their energies, the $\nu(1g_{9/2})^2$ and $\pi(1g_{9/2})^2$ configurations were obtained. Their excitation energies with respect to the ground state are about 2.0 and 11.8 MeV, respectively. As can be seen from the experimental level scheme (Fig. 2) and following arguments outlined in Sec. III, the band head energy of Band 1 is greater than 10 MeV at $I^\pi \geq 12^+$. Thus, within this framework, Band 1 is assigned the $\pi(1g_{9/2})^2$ configuration with deformation parameters of $\beta = 0.20$ and $\gamma = 45.9^\circ$.

With the configuration and deformation parameters obtained from the adiabatic and configuration-fixed constrained covariant density functional theory, single- j shell quantum particle rotor model [42–44] calculations were performed to further examine the energy spectra for band 1. For this purpose, the irrotational flow type of moment of inertia $\mathcal{J}_k = \mathcal{J}_0 \sin^2(\gamma - 2k\pi/3)$ with $\mathcal{J}_0 = 19.0 \hbar^2/\text{MeV}$ was adopted. The energy spectra obtained as function of spin are compared in Fig. 13 with the experimental data. Clearly, the theoretical calculations are able to reproduce the data and support the configuration assignment of $\pi(1g_{9/2})^2$ to Band 1.

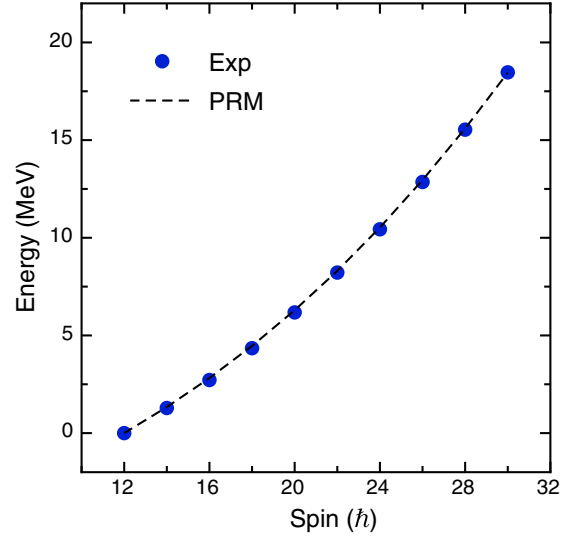


FIG. 13. Energy as a function of spin for the rotational band (Band 1) in ^{66}Zn calculated by particle rotor model in comparison with the experimental data.

In Fig. 14, the root mean square components along the medium (m -), short (s -), and long (l -) axes of the core $R_k = \langle \hat{R}_k^2 \rangle^{1/2}$, the active protons $J_{\pi k} = \langle \hat{j}_{pk}^2 \rangle^{1/2}$, and the total nuclear system $I_k = \langle \hat{I}_k^2 \rangle^{1/2}$ are displayed as functions of spin when calculated for Band 1 by means of the particle rotor model. As can be seen, the angular momentum of the collective core is mainly aligned along the m axis, which corresponds to the largest moment of inertia. It is noted that the l -axis component cannot be neglected in the low spin region. The angular momentum of the $g_{9/2}$ active proton particles mainly align along the s axis with a value of about $7.5\hbar$ at the band head, which corresponds to maximal overlap with the triaxial core [46]. With increasing spin, the protons tend to align gradually along the m -axis, which is attributed to the fact that the core induces a strong Coriolis force to the proton particles and tries

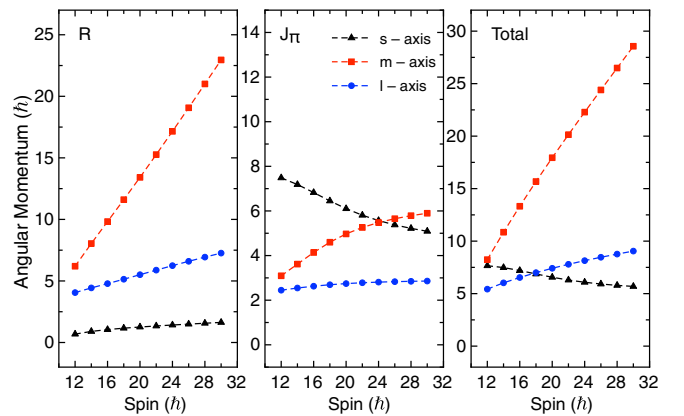


FIG. 14. The root mean square components along the medium (m), short (s), and long (l) axis of the core $R_k = \langle \hat{R}_k^2 \rangle^{1/2}$, the active protons $J_{\pi k} = \langle \hat{j}_{pk}^2 \rangle^{1/2}$, and the total nuclear system $I_k = \langle \hat{I}_k^2 \rangle^{1/2}$ as function of spin calculated by means of particle rotor model for the Band 1 in ^{66}Zn .

to align them along the m -axis to minimize energy. As a result, the angular momentum of the total nuclear system has comparable components along the three principal axes in the low spin region. At high spin, however, the nucleus aligns along the m -axis, which is, in fact, the principal axis of rotation and leads naturally to the observed $\Delta I = 2$ quadrupole band structure.

Within the present theoretical framework, the properties of Band 1 are accounted for without invoking the large deformation inferred on the basis of comparisons with bands in other Zn isotopes and the ^{68}Ge isotone. It should be noted, however, that just as in the present case, there is no lifetime information available for the SD bands in ^{68}Ge and ^{65}Zn . The interpretation in terms of extended shapes relies on striking similarities with bands in other Zn isotopes where lifetimes data are available as well as on theoretical approximations which differ from those discussed above. Hence, it is clear that further progress regarding the description of the ^{66}Zn band and the associated nuclear shape will have to await additional lifetime measurements. The latter will likely be challenging in view of the small intensity (less than 10% relative to the ground-state band) with which the band is fed, at least with the reaction used in the present measurements. Furthermore, a comparison of calculations within the CDFT/PRM framework presented in this study with the data on the other sequences observed in nuclei of the region, which were interpreted in earlier works as superdeformed bands, would be of considerable interest.

V. CONCLUSIONS

Medium and high-spin states in ^{66}Zn have been investigated by means of the complex multinucleon transfer reaction, $^{26}\text{Mg}(^{48}\text{Ca}, \alpha 4n\gamma)$, carried out at beam energies of 275, 290, and 320 MeV in inverse kinematics. The previously reported low-spin structure was essentially confirmed. Large-scale shell-model calculations carried out using the JUN45 and jj44b effective interactions have successfully described the observations and confirmed the view that the low-lying levels in this nucleus and in other neighboring nuclei of the

region are mostly associated with single particle-hole excitations. In addition, evidence for a new, high-spin rotational sequence of stretched- $E2$ transitions has been observed in coincidence with the known low-spin states. Due to difficulties in identifying linking transitions between the newly established sequence and the low-spin levels, presumably because of the low in-band intensity and the fragmented decay paths, the excitation energies of the levels, the spins and parity could not be determined. The band is, however, observed to share striking similarities with rotational cascades associated with superdeformation in neighboring $A \approx 60$ – 70 nuclei. Calculations, carried out within the framework of the adiabatic and configuration-fixed constrained covariant density functional theory and the quantum particle rotor model, suggest an associated configuration involving two proton particles occupying the $g_{9/2}$ intruder orbital. Within this theoretical framework, the band is associated with triaxial deformation. Further data will be required to firmly establish the associated nuclear shape. Nevertheless, it is clear that despite the limited number of orbitals present near the Fermi surface, nuclei of the $A \approx 60$ – 70 mass region display a rich diversity of phenomena similar to those seen in heavier mass systems and, in particular, exhibit strong collectivity at high spins.

ACKNOWLEDGMENTS

The authors thank J. P. Greene (ANL) for target preparation and the ATLAS operations staff for the efficient running of the accelerator during the experiment. The authors also gratefully acknowledge contributions from C. J. Lister, B. DiGiovine, and T. Baugher. This material is based upon work supported by the U.S. Department of Energy, Office of Science, Office of Nuclear Physics under Contract under Contract No. DE-AC02-06CH11357 and Grants No. DE-FG02-94ER40834, No. DE-FG02-08ER41556, and No. DE-SC0020451 and by the National Science Foundation under Contract No. PHY-0606007, and by the UNC Startup Funds of ADA. This research used resources of ANL's ATLAS facility, which is a DOE Office of Science User Facility.

-
- [1] C. Andreoiu, D. Rudolph, C. E. Svensson, A. V. Afanasjev, J. Dobaczewski, I. Ragnarsson, C. Baktash, J. Eberth, C. Fahlander, D. S. Haslip, D. R. LaFosse, S. D. Paul, D. G. Sarantites, H. G. Thomas, J. C. Waddington, W. Weintraub, J. N. Wilson, and C.-H. Yu, *Phys. Rev. C* **62**, 051301(R) (2000).
- [2] D. Rudolph, C. Baktash, J. Dobaczewski, W. Nazarewicz, W. Satuła, M. J. Brinkman, M. Devlin, H.-Q. Jin, D. R. LaFosse, L. L. Riedinger, D. G. Sarantites, and C.-H. Yu, *Phys. Rev. Lett.* **80**, 3018 (1998).
- [3] C. E. Svensson, D. Rudolph, C. Baktash, M. A. Bentley, J. A. Cameron, M. P. Carpenter, M. Devlin, J. Eberth, S. Flibotte, A. Galindo-Uribarri, G. Hackman, D. S. Haslip, R. V. F. Janssens, D. R. LaFosse, T. J. Lampman, I. Y. Lee, F. Lerma, A. O. Macchiavelli, J. M. Nieminen, S. D. Paul *et al.*, *Phys. Rev. Lett.* **82**, 3400 (1999).
- [4] C.-H. Yu, C. Baktash, J. Dobaczewski, J. A. Cameron, C. Chitu, M. Devlin, J. Eberth, A. Galindo-Uribarri, D. S. Haslip, D. R. LaFosse, T. J. Lampman, I.-Y. Lee, F. Lerma, A. O. Macchiavelli, S. D. Paul, D. C. Radford, D. Rudolph, D. G. Sarantites, C. E. Svensson, J. C. Waddington *et al.*, *Phys. Rev. C* **60**, 031305(R) (1999).
- [5] C.-H. Yu, C. Baktash, J. Dobaczewski, J. A. Cameron, M. Devlin, J. Eberth, A. Galindo-Uribarri, D. S. Haslip, D. R. LaFosse, T. J. Lampman, I.-Y. Lee, F. Lerma, A. O. Macchiavelli, S. D. Paul, D. C. Radford, D. Rudolph, D. G. Sarantites, C. E. Svensson, J. C. Waddington, and J. N. Wilson, *Phys. Rev. C* **62**, 041301(R) (2000).
- [6] M. Devlin, A. V. Afanasjev, R. M. Clark, D. R. LaFosse, I. Y. Lee, F. Lerma, A. O. Macchiavelli, R. W. MacLeod, I. Ragnarsson, P. Ring, D. Rudolph, D. G. Sarantites, and P. G. Thirolf, *Phys. Rev. Lett.* **82**, 5217 (1999).
- [7] D. Rudolph, C. Baktash, M. Devlin, D. R. LaFosse, L. L. Riedinger, D. G. Sarantites, and C.-H. Yu, *Phys. Rev. Lett.* **86**, 1450 (2001).

- [8] C. E. Svensson, C. Baktash, J. A. Cameron, M. Devlin, J. Eberth, S. Flibotte, D. S. Haslip, D. R. LaFosse, I. Y. Lee, A. O. Macchiavelli, R. W. MacLeod, J. M. Nieminen, S. D. Paul, L. L. Riedinger, D. Rudolph, D. G. Sarantites, H. G. Thomas, J. C. Waddington, W. Weintraub, J. N. Wilson *et al.*, *Phys. Rev. Lett.* **79**, 1233 (1997).
- [9] C. E. Svensson, C. Baktash, G. C. Ball, J. A. Cameron, M. Devlin, J. Eberth, S. Flibotte, A. Galindo-Uribarri, D. S. Haslip, V. P. Janzen, D. R. LaFosse, I. Y. Lee, A. O. Macchiavelli, R. W. MacLeod, J. M. Nieminen, S. D. Paul, D. C. Radford, L. L. Riedinger, D. Rudolph, D. G. Sarantites *et al.*, *Phys. Rev. Lett.* **80**, 2558 (1998).
- [10] A. Galindo-Uribarri, D. Ward, G. C. Ball, V. P. Janzen, D. C. Radford, I. Ragnarsson, and D. Headly, *Phys. Lett. B* **422**, 45 (1998).
- [11] C.-H. Yu, C. Baktash, J. A. Cameron, M. Devlin, J. Eberth, A. Galindo-Uribarri, D. S. Haslip, D. R. LaFosse, T. J. Lampman, I.-Y. Lee, F. Lerma, A. O. Macchiavelli, S. D. Paul, D. C. Radford, I. Ragnarsson, D. Rudolph, D. G. Sarantites, C. E. Svensson, J. C. Waddington, J. C. Wells *et al.*, *Phys. Rev. C* **65**, 061302(R) (2002).
- [12] D. Ward, C. E. Svensson, I. Ragnarsson, C. Baktash, M. A. Bentley, J. A. Cameron, M. P. Carpenter, R. M. Clark, M. Cromaz, M. A. Deleplanque, M. Devlin, R. M. Diamond, P. Fallon, S. Flibotte, A. Galindo-Uribarri, D. S. Haslip, R. V. F. Janssens, T. Lampman, G. J. Lane, I. Y. Lee *et al.*, *Phys. Rev. C* **63**, 014301 (2000).
- [13] A. Gade, H. Klein, N. Pietralla, and P. von Brentano, *Phys. Rev. C* **65**, 054311 (2002).
- [14] R. Schwengner, R. Massarczyk, M. Scheck, W. Tornow, G. Battaglia, T. Beck, D. Bemmerer, N. Benouaret, R. Beyer, M. Butterling, F. Fiedler, S. W. Finch, C. Fransen, U. Friman-Gayer, A. Frotscher, R. Gonzalez, M. Grieger, A. Hartmann, T. Hensel, E. Hoemann *et al.*, *Phys. Rev. C* **103**, 024312 (2021).
- [15] P. M. Endt and C. Alderliesten, *Nucl. Phys. A* **575**, 297 (1994).
- [16] G. F. Neal, Z. P. Sawa, F. P. Venezia, and P. R. Chagnon, *Nucl. Phys. A* **280**, 161 (1977).
- [17] J. Leske, K.-H. Speidel, S. Schielke, J. Gerber, P. Maier-Komor, T. Engeland, and M. Hjorth-Jensen, *Phys. Rev. C* **73**, 064305 (2006).
- [18] J. F. Bruandet, M. Agard, A. Giorni, J. P. Longequeue, C. Morand, and T. U. Chan, *Phys. Rev. C* **12**, 1739 (1975).
- [19] M. Rocchini, K. Hadyńska-Klęk, A. Nannini, A. Goasduff, M. Zielińska, D. Testov, T. R. Rodríguez, A. Gargano, F. Nowacki, G. De Gregorio, H. Naïdja, P. Sona, J. J. Valiente-Dobón, D. Mengoni, P. R. John, D. Bazzacco, G. Benzoni, A. Boso, P. Cocconi, M. Chiari *et al.*, *Phys. Rev. C* **103**, 014311 (2021).
- [20] I. Bala, S. C. Pancholi, M. K. Raju, A. Dhal, S. Saha, J. Sethi, T. Trivedi, R. Raut, S. S. Ghugre, R. Palit, R. P. Singh, and S. Muralithar, *Phys. Rev. C* **104**, 044302 (2021).
- [21] S. Rai, U. S. Ghosh, B. Mukherjee, A. Biswas, A. K. Mondal, K. Mandal, A. Chakraborty, S. Chakraborty, G. Mukherjee, A. Sharma, I. Bala, S. Muralithar, and R. P. Singh, *Phys. Rev. C* **102**, 064313 (2020).
- [22] R. V. F. Janssens and F. Stephens, *Nucl. Phys. News* **6**, 9 (1996).
- [23] I.-Y. Lee, *Nucl. Phys. A* **520**, c641 (1990).
- [24] M. Albers, S. Zhu, R. V. F. Janssens, J. Gellanki, I. Ragnarsson, M. Alcorta, T. Baugher, P. F. Bertone, M. P. Carpenter, C. J. Chiara, P. Chowdhury, A. N. Deacon, A. Gade, B. DiGiovine, C. R. Hoffman, F. G. Kondev, T. Lauritsen, C. J. Lister, E. A. McCutchan, D. S. Moerland *et al.*, *Phys. Rev. C* **88**, 054314 (2013).
- [25] D. C. Radford, *Nucl. Instrum. Methods Phys. Res. A* **361**, 297 (1995).
- [26] Gammasphere Documentation - Detector Angles, <http://www.phy.anl.gov/gammasphere/doc/detector-angles.html>, Accessed: 03-30-2015.
- [27] N. Sensharma, Wobbling motion in nuclei: Transverse, longitudinal and chiral, Ph.D. thesis, University of Notre Dame, 2021.
- [28] J. F. A. Van Hienen, W. Chung, and B. H. Wildenthal, *Nucl. Phys. A* **269**, 159 (1976).
- [29] A. Boucenna, L. Kraus, I. Linck, and T. U. Chan, *Phys. Rev. C* **42**, 1297 (1990).
- [30] D. P. Ahalpara, K. H. Bhatt, S. P. Pandya, and C. R. Praharaj, *Nucl. Phys. A* **371**, 210 (1981).
- [31] V. Lopac and V. Paar, *Nucl. Phys. A* **297**, 471 (1978).
- [32] L. Cleemann, J. Eberth, W. Neumann, and V. Zobel, *Nucl. Phys. A* **386**, 367 (1982).
- [33] S. K. Sharma, *Phys. Rev. C* **22**, 2612 (1980).
- [34] B. Brown and W. Rae, *Nucl. Data Sheets* **120**, 115 (2014).
- [35] L. C. McIntyre, *Phys. Rev.* **152**, 1013 (1966).
- [36] M. G. Betigeri, P. David, J. Debrus, H. Mommsen, and A. Riccato, *Nucl. Phys. A* **171**, 401 (1971).
- [37] J. Dudek, W. Nazarewicz, Z. Szymanski, and G. A. Leander, *Phys. Rev. Lett.* **59**, 1405 (1987).
- [38] R. Bengtsson, S. Frauendorf, and F.-R. May, *At. Data Nucl. Data Tables* **35**, 15 (1986).
- [39] J. Meng, J. Peng, S. Q. Zhang, and S.-G. Zhou, *Phys. Rev. C* **73**, 037303 (2006).
- [40] J. Meng, J.-Y. Guo, J. Li, Z. Li, H. Liang, W. Long, Y. Niu, Z. Niu, J. Yao, Y. Zhang *et al.*, *Prog. Phys.* **31**, 199 (2011).
- [41] J. Meng, *Relativistic Density Functional for Nuclear Structure* (World Scientific, Singapore, 2016).
- [42] E. Streck, Q. B. Chen, N. Kaiser, and Ulf-G. Meißner, *Phys. Rev. C* **98**, 044314 (2018).
- [43] Q. B. Chen, S. Frauendorf, and C. M. Petrache, *Phys. Rev. C* **100**, 061301(R) (2019).
- [44] Q. B. Chen, S. Frauendorf, N. Kaiser, U.-G. Meißner, and J. Meng, *Phys. Lett. B* **807**, 135596 (2020).
- [45] P. W. Zhao, Z. P. Li, J. M. Yao, and J. Meng, *Phys. Rev. C* **82**, 054319 (2010).
- [46] S. Frauendorf and J. Meng, *Z. Phys. A: Hadrons Nucl.* **356**, 263 (1996).